Gold Nanobipyramid-Directed Growth of Length-Variable Silver Nanorods with Multipolar Plasmon Resonances

Xiaolu Zhuo,[†] Xingzhong Zhu,[†,‡] Qian Li,[†] Zhi Yang,[*,‡] and Jianfang Wang[*,†]

[†]Department of Physics, The Chinese University of Hong Kong, Shatin, Hong Kong SAR, China and [‡]Key Laboratory for Thin Film and Microfabrication of Ministry of Education, Department of Micro/Nano Electronics, School of Electronic Information and Electrical Engineering, Shanghai Jiao Tong University, Shanghai 200240, China

ABSTRACT We report on a method for the preparation of uniform and length-variable Ag nanorods through anisotropic Ag overgrowth on high-purity Au nanobipyramids. The rod diameters can be roughly tailored from ~20 nm to ~50 nm by judicious selection of differently sized Au nanobipyramids. The rod lengths can be tuned from ~150 nm to ~550 nm by varying the Ag precursor amount during the overgrowth process and/or by anisotropic shortening through mild oxidation. The controllable aspect ratios, high purity, and high dimensional uniformity of these Ag nanorods enable the observation of Fabry–Pérot-like multipolar plasmon resonance modes in the colloidal suspensions at the ensemble level, which has so far been demonstrated only on Au nanorods prepared electrochemically with anodic aluminum oxide templates. Depending on the mode order and geometry of the Ag nanorods, the multipolar plasmon wavelengths can be readily tailored over a wide spectral range from the visible to near-infrared region. We have further elucidated the relationships between the multipolar plasmon wavelengths and the geometric dimensions of the Ag nanorods at both the ensemble and single-particle levels. Our results indicate that the Au nanobipyramid-directed, dimensionally controllable Ag nanorods will be an attractive and promising candidate for developing multipolar plasmon-based devices and applications.

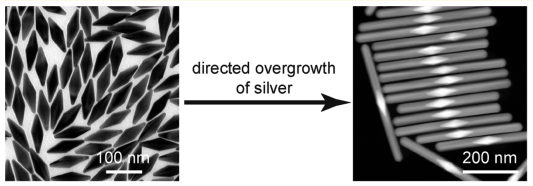

KEYWORDS: gold nanobipyramids · multipolar plasmon resonance · plasmon resonance · scattering · seed-mediated growth · silver nanorods

Gold and silver nanostructures have been receiving intensive attention because of their easy manipulation of localized surface plasmon resonance at visible and near-infrared frequencies and their extensive applications in nanophotonics,[1] chemical/biological sensing,[2] photocatalysis,[3] and surface-enhanced spectroscopies.[4] Recently, much interest has been aroused in multipolar plasmon resonance modes owing to their unique plasmonic properties, which are distinct from those of dipolar plasmon resonance modes.[5−7] High-aspect-ratio elongated metal nanostructures, such as high-aspect-ratio nanorods and nanorices, can support multipolar plasmon resonance modes, which are similar to the standing waves in Fabry–Pérot resonators.[8−12] The dependences of the multipolar plasmon resonance wavelengths on the rod dimensions make them an ideal platform for studying multipolar plasmon behaviors as well as for further exploring multipolar plasmon-based optical devices and various technological applications.

Over the past decade, much effort has been made on understanding the nature of multipolar plasmon modes supported by high-aspect-ratio metal nanostructures. A number of theoretical works have been performed on identifying the resonance frequencies of the multipolar plasmon resonance modes that are supported by Au and Ag nanorods using different methods.[13,14] In addition, theoretical and experimental investigations have revealed that multipolar plasmon resonance possesses narrower line widths than dipolar plasmon resonance due to its lower radiative damping.[6,14] The narrower line widths are beneficial to the development of ultrasensitive plasmonic chemical/biological sensors,[15] low-threshold nanolasers, and low-loss waveguides.[16] Recently, the Fano-like line shape of multipolar plasmon resonance has attracted particular attention as a medium for understanding

* Address correspondence to jfwang@phy.cuhk.edu.hk, zhiyang@sjtu.edu.cn.

Received for review May 1, 2015 and accepted July 2, 2015.

Published online July 02, 2015
10.1021/acsnano.5b02622

plasmonic interference phenomena.[7,17,18] Furthermore, multipolar plasmon modes of different orders show distinct radiation properties,[5,19] which opens new possibilities for light manipulation, nanoantenna design, and fluorescence control.[20,21] These unique properties of multipolar plasmon resonance create many new opportunities for nanoplasmonic and nanophotonic applications.[22]

To date, the multipolar plasmon modes of high-aspect-ratio metal nanostructures have been experimentally observed mainly in two ways. One relies on optical spectroscopy, which is performed at the ensemble level on lithographically fabricated metal nanoparticle arrays.[23,24] The other is carried out at the single-particle level, by dark-field scattering spectroscopy,[6,25] electron energy-loss spectroscopy,[8−10,18] photoemission electron microscopy,[11] scanning near-field optical microscopy,[12,26] and polarization contrast microscopy.[27] So far, there has been only one experimental observation in colloidal suspensions at the ensemble level, which is made on electrochemically fabricated Au nanorods with anodic aluminum oxide templates.[28] The main reason for the rare experimental observation of multipolar plasmon resonance at the ensemble level is that most high-aspect-ratio metal nanostructures reported so far have relatively large length distributions.[29−32] The peaks of the multipolar plasmon modes are severely broadened inhomogeneously and become unobservable, which causes difficulties in studying multipolar plasmon modes, in synthetically tailoring multipolar plasmon wavelengths, and in developing multipolar plasmon-based devices and metamaterials through assembly. Therefore, it is strongly desirable to invent methods for the synthesis of highly uniform high-aspect-ratio metal nanostructures.

Herein, we present a method for the preparation of size-controllable and highly uniform Ag nanorods in high yields through anisotropic Ag overgrowth on Au nanobipyramids (NBPs). The diameters and lengths of the Au NBP-directed Ag nanorods can be tailored independently. By using Au NBPs of different sizes as cores, the diameters of the obtained Ag nanorods can be roughly controlled from ~20 nm to ~50 nm. For Ag nanorods with fixed diameters, their lengths can be readily varied from ~150 nm to ~550 nm by increasing the amount of the Ag precursor in the overgrowth process. Through our synthetic size control, the wavelength of each multipolar plasmon mode is tunable from the visible to near-infrared region. The high purity and high size uniformity of these Ag nanorods have allowed us to observe well-separated multipolar plasmon modes in their colloidal suspensions at the ensemble level. The obtained relationships between the multipolar plasmon wavelengths and the rod length are corroborated by and consistent with those from single-particle dark-field scattering spectroscopy. The dependences of the multipolar plasmon wavelengths on the rod length obtained in our experiments are consistent with the previous empirical description and supported by electrodynamic simulations. In addition, our as-prepared Ag nanorods can be precisely shortened through anisotropic mild oxidation, which offers an alternative means for finely tailoring the multipolar plasmon peak positions. Furthermore, our Au NBP-directed Ag nanorods can also be converted into other interesting nanostructures, such as size-controllable hollow AuAg nanostructures and Ag nanowires.

RESULTS AND DISCUSSION

Gold NBP-Directed Growth of Silver Nanorods. We employed a stepwise combination of seed-mediated growth of Au NBPs and Ag overgrowth to produce Ag nanorods, as schematically illustrated in Figure 1a. First, penta-twinned Au NBPs were obtained from seed-mediated growth in aqueous solutions with cetyltrimethylammonium bromide (CTAB) as the stabilizing agent.[33,34] We have described in our previous study[35] depletion-induced separation for producing monodisperse Au NBPs with number purities approaching 100%. The ensemble spectral line widths of the Au NBP samples are almost the same as the average line widths obtained from single-particle measurements,

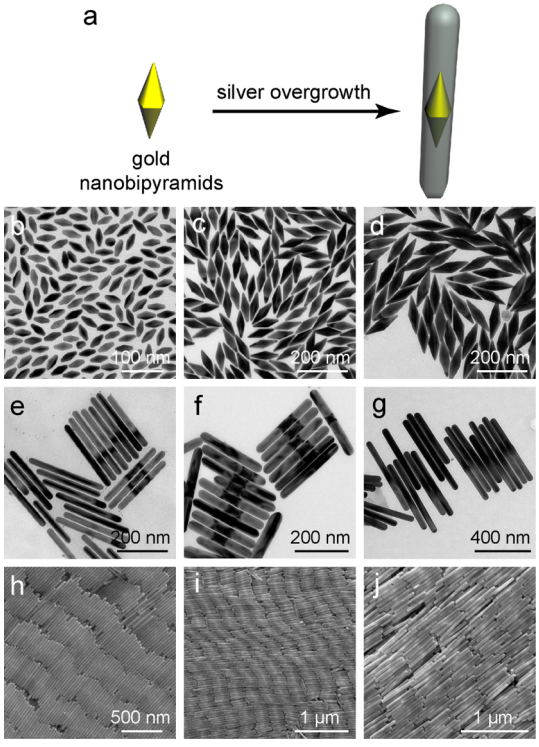

Figure 1. Gold NBP-directed growth of silver nanorods with diameter control. (a) Schematic illustrating the anisotropic Ag overgrowth on Au NBPs. (b−d) TEM images of the 650, 800, and 900 nm NBP samples, respectively. (e−g) TEM images of the Ag nanorod samples grown from the 650, 800, and 900 nm NBP samples, respectively. (h−j) Corresponding SEM images of the three Ag nanorod samples.

suggesting that our Au NBP samples are highly uniform in shape and size. By varying the volume ratio between the seed and growth solutions, Au NBPs of different sizes were obtained. We subsequently carried out anisotropic Ag overgrowth on the high-purity Au NBPs in the presence of cetyltrimethylammonium chloride (CTAC).[36] $AgNO_3$ and ascorbic acid were used as the Ag precursor and reducing agent, respectively. The produced Ag nanorods, with Au NBP cores located at the center, also possess pentagonal symmetry, as characterized previously.[33,36,37] Similar to penta-twinned Ag nanowires, Ag deposition leads to the formation of the {100} facets on the side surfaces of the Ag nanorods and the {111} facets at the two ends.[37] Due to the adsorption of the halide−surfactant complexes, the stability of the {100} facets is enhanced.[38] In addition, the packing density of CTAC molecules is smaller at the two ends of the Ag nanorods, leaving the {111} facets more exposed for reactions with species in solutions.[39] Consequently, anisotropic overgrowth is maintained along the longitudinal direction. Proper choice of Au NBPs can roughly determine the diameters of the resultant Ag nanorods. During the overgrowth process, the depletion force-induced attractive potential between the Ag nanorods becomes larger with increasing lengths, resulting in the formation of flocculation and subsequent gravitational sedimentation.[40] The flocculation can be eliminated after overgrowth by reducing the surfactant concentration but is unavoidable during the overgrowth process. We therefore employed an air-bath shaker to prevent sedimentation of the flocculation in the growth solution. We found that shaking during overgrowth is crucial for avoiding the size nonuniformity caused by flocculation-induced sedimentation. In this step, the lengths of the Ag nanorods can be readily controlled by varying the amount of the Ag precursor. If very long Ag nanorods or Ag nanowires are desired, the Ag precursor should be added in multiple aliquots to avoid the production of irregularly shaped Ag nanoparticle impurities through self-nucleation and subsequent growth.[41]

We first demonstrate that the diameters of the Ag nanorods can be approximately controlled with our method by judiciously choosing Au NBPs of different sizes as the cores. Three Au NBP samples with longitudinal plasmon wavelengths of 650, 800, and 900 nm, respectively, were prepared for use as the cores to direct Ag overgrowth. The three Au NBP samples are hereinafter referred to as 650, 800, and 900 nm NBPs. Their transmission electron microscopy (TEM) and scanning electron microscopy (SEM) images are shown in Figure 1b−d and Supporting Information Figure S1. The average lengths/waist diameters, measured from the TEM images, are 43 ± 2 nm/19 ± 1 nm, 110 ± 4 nm/35 ± 1 nm, and 156 ± 5 nm/45 ± 2 nm, respectively. The highly uniform sizes and shapes of these Au NBP samples, as revealed by TEM and SEM imaging, are essential for the preparation of uniformly sized Ag nanorods. The Ag nanorod samples directed by the three Au NBP samples are displayed in the TEM and SEM images in Figure 1e−j. The obtained Ag nanorods possess uniform dimensions, with their average lengths/diameters determined from TEM imaging to be 286 ± 28 nm/27 ± 1 nm, 282 ± 23 nm/38 ± 1 nm, and 549 ± 41 nm/48 ± 2 nm, respectively. As will be shown below, the lengths of the Ag nanorods can be controlled by varying the Ag precursor amount. On the other hand, the average diameters of the Ag nanorod samples are slightly larger than those of the corresponding Au NBP samples. For each sample, the standard deviation is within 5% of the average diameter. It is similar to that of the corresponding Au NBP sample. Although the exact dimensional relationship between the resultant Ag nanorods and the directing Au NBPs remains elusive, which is due to the limitation in producing Au NBPs with well-controlled diameters over a wide range, our results indicate clearly that the diameters of the Ag nanorods can be varied by use of differently sized Au NBPs.

We next show that the lengths of the Ag nanorods can be facilely controlled by changing the Ag precursor amount during the overgrowth process. The 800 nm NBP sample with an average diameter of 35 nm was employed as an example for this purpose. Five Ag nanorod samples were prepared under the same conditions except that the supplied amounts of $AgNO_3$ and ascorbic acid were varied. Figure 2 shows the TEM and SEM images of these Ag nanorod samples. Each Ag nanorod is uniform in diameter along the length direction. The average diameters of the 5 nanorod samples are all 38 ± 1 nm. The average lengths are 168 ± 9, 227 ± 16, 282 ± 23, 397 ± 36, and 556 ± 46 nm, respectively. As a result, the aspect ratios of these Ag nanorods are increased from ~5 to ~16. For each sample, the standard deviation relative to the average length is within 10%. By combining our synthetic controllability on diameter and length, Ag nanorods with aspect ratios ranging from ~3 to ~30 can be readily produced.

To further verify the Au NBP-directed growth of Ag nanorods, we performed high-angle annular dark-field scanning transmission electron microscopy (HAADF-STEM) imaging and elemental mapping on the Ag nanorods (Supporting Information Figure S2). The Au NBPs were observed to be embedded within the Ag nanorods. For a majority of the Ag nanorods, the Au NBPs were found to be located at the center of the Ag nanorods, suggesting that the preferential Ag overgrowth along the length direction is symmetric at the two ends. However, there do exist Ag nanorods with the Au NBPs being located off center. Interestingly, the Ag nanorods with off-centered Au NBPs are comparable in length to those with exactly centered Au NBPs. We have not understood the growth behavior

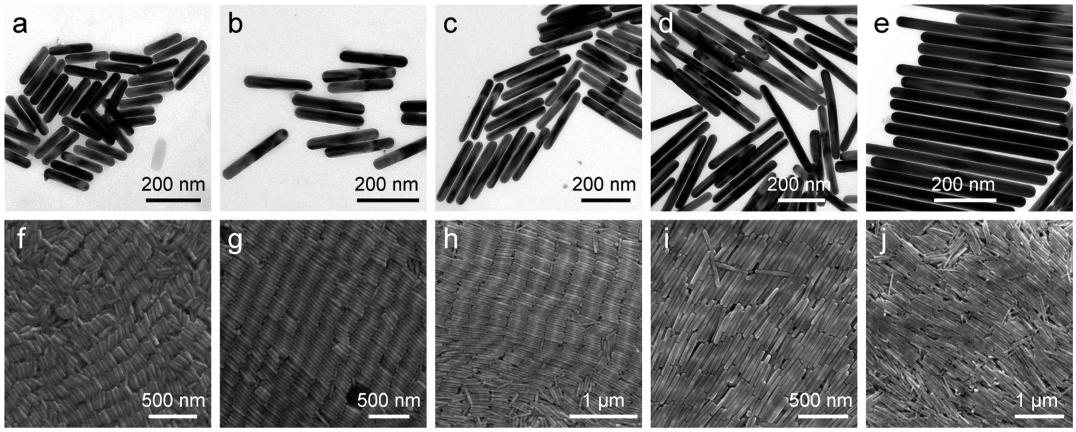

Figure 2. Au NBP-directed growth of Ag nanorods with length control. (a−e) TEM and (f−j) corresponding SEM images of the 5 Ag nanorod samples using the 800 nm NBPs as the cores.

of the off-centered Ag nanorods. Understanding it might lead to the synthesis of many types of asymmetric bimetallic nanostructures with interesting plasmonic and catalytic properties.

Multipolar Plasmon Resonance. We first measured and analyzed the extinction spectra of the ensemble Ag nanorod samples with a spectrophotometer to examine their multipolar plasmon resonance modes because of the simplicity and ease of ensemble extinction measurements. Figure 3a displays the extinction spectra of the three Ag nanorod samples with different diameters as shown in Figure 1, together with those of the three directing Au NBP samples. Figure 3b shows the extinction spectra of the 5 Ag nanorod samples with different lengths as shown in Figure 2. As reported in our previous work,[35] the Au NBP samples exhibit a strong longitudinal dipolar plasmon peak and two or three weak peaks in the higher-energy region, depending on the NBP size. The weak peaks arise from the transverse dipolar plasmon mode and longitudinal higher-order plasmon modes. Upon Ag overgrowth, two prominent peaks were observed (Figure 3a). They come from the transverse plasmon mode and longitudinal dipolar plasmon mode, respectively. In addition, there appears a shoulder peak around 350 nm on the higher-energy side of the transverse plasmon peak. This peak is attributed to the plasmon resonance of bulk silver.[42] In between these two strong peaks, there exist multiple weak peaks, whose number is dependent on the nanorod length. To better understand the occurrence of the weak peaks, we carefully examined the extinction spectra of the 5 Ag nanorod samples that had the same diameter. When the Ag nanorods are relatively short (sample 1 in Figure 3b), there are mainly two extinction peaks, which correspond to the transverse and longitudinal dipolar plasmon modes, respectively. As the length is increased, the longitudinal dipolar plasmon peak red-shifts and additional peaks appear in between the transverse and longitudinal dipolar plasmon peaks. These additional peaks originate from multipolar plasmon modes of different orders, as will be discussed below. Similar peaks have also been seen from other elongated ensemble metal nanostructure samples, but usually as a broad shoulder near the longitudinal dipolar plasmon peak.[25,30,32] In our work, it is the high aspect ratios, high purity, and high dimensional uniformity of the Ag nanorods that allow for the observation of the well-separated multipolar plasmon peaks in the colloidal ensemble suspensions. Little overlap between the adjacent peaks is beneficial to multipolar plasmon-based applications.

Finite-difference time-domain (FDTD) simulations were performed to ascertain the nature of each plasmon band. According to the geometry of sample 2 in Figure 3b, the rod length and diameter were set to 226 and 38 nm, respectively, in the simulations. In particular, since we were curious about the effect of the Au NBP core, we considered the Ag nanorod with and without the Au NBP core for comparison (Supporting Information Figures S3 and S4), where the Au NBP core has a length of 110 nm and a waist diameter of 35 nm. Excitation light with varying incidence angles relative to the rod length axis and different polarizations were taken into consideration because the modes with even parity can be excited only by incident light non-normal to the length axis.[7,25] Once the extinction spectra for all combinations of the incidence angles and polarizations were obtained, the average extinction cross-section spectrum was calculated by multiplying each spectrum with its occurrence probability and then adding them all together. Figure 3c shows the simulated extinction cross-section spectra of the Au-NBP-cored Ag nanorod and the pure Ag nanorod, together with the experimental extinction spectrum. In general, the peak positions of the three spectra match well with each other except for those around 500 nm (black and red curves in Figure 3c). The broader line widths of the measured plasmon peaks result from the remaining inhomogeneous broadening of the ensemble Ag nanorod sample even though the Ag nanorods are

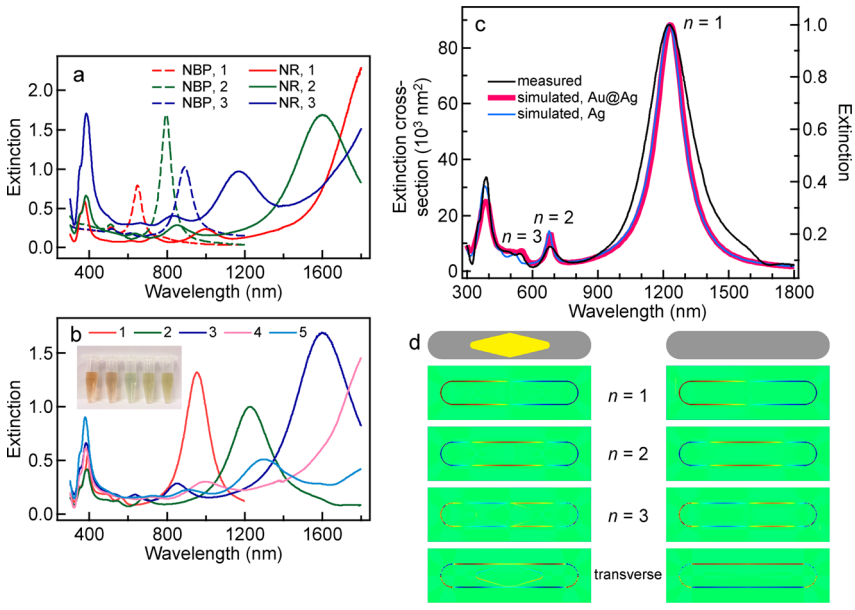

Figure 3. Extinction spectra and FDTD simulations of the Au NBP-directed Ag nanorods. (a) Experimental extinction spectra of the Au NBP samples and the corresponding Ag nanorod samples with different diameters. The longitudinal plasmon wavelengths of the Au NBP samples 1, 2, and 3 are 650, 800, and 900 nm, respectively, with the resultant Ag nanorod samples labeled as 1, 2, and 3, correspondingly. (b) Experimental extinction spectra of the Ag nanorod samples with different lengths. The nanorod samples were grown from the 800 nm NBP sample. The inset shows a photograph of samples 1 to 5 from left to right. The spectra beyond the wavelength of 1300 nm were measured with D_2O. (c) Simulated extinction cross-section spectra of the Au-NBP-cored Ag nanorod and the pure Ag nanorod, together with the measured extinction spectrum. (d) Charge distribution contours of the Au-NBP-cored Ag nanorod (left) and the pure Ag nanorod (right). From top to bottom, the wavelengths of the considered peaks are 1231, 680, 551, and 380 nm for the Au-NBP-cored Ag nanorod and 1227, 677, 522, and 372 nm for the pure Ag nanorod, respectively. For the $n = 1$ and $n = 3$ peaks, the excitation light is incident perpendicularly to and polarized along the rod length axis. For the transverse plasmon peak, the excitation light is both incident and polarized perpendicularly to the length axis. For the $n = 2$ peak, the excitation light is incident at an angle of 45° relative to the length axis and polarized in the plane determined jointly by the incident light wavevector and the rod length axis.

highly uniform in size. The four plasmon bands from low to high energies, corresponding to the longitudinal dipolar plasmon mode ($n = 1$), longitudinal quadrupolar plasmon mode ($n = 2$), longitudinal octupolar plasmon mode ($n = 3$), and transverse dipolar plasmon mode, respectively, were identified from their charge distribution contours shown in Figure 3d. Our previous study has shown that in (Au core)@(Ag shell) nanostructures the effect of the Au core on the plasmon bands is completely screened by the Ag shell when the shell thickness is larger than 5 nm.[43] For the Ag nanorod sample considered in Figure 3c, the Ag shell thicknesses on the tips of the Au NBPs are larger than 5 nm, while those on the sides are smaller than 5 nm. As a result, the effect of the Au NBP core on the longitudinal plasmon modes is insignificant, whereas the plasmon coupling between the Au NBP core and the Ag shell in the transverse direction gives rise to a shoulder around 500 nm (black and red curves in Figure 3c). Since the $n = 3$ peak is also located around 500 nm, its coupling with the transverse plasmon mode of the Au NBP core causes a slight red shift of the $n = 3$ peak. Nevertheless, the simulated spectrum and charge distributions of the Au-NBP-cored Ag nanorod are very similar to those of the pure Ag nanorod, suggesting that the Au NBP core has little effect on the plasmonic behavior of the Ag nanorod. Therefore, it is safe to simply treat the Au-NBP-cored Ag nanorods as pure Ag nanorods plasmonically.

There is an analogy between the multipolar plasmon modes supported by the high-aspect-ratio Ag nanorods and the optical standing waves in Fabry–Pérot cavities. A single metal nanorod can be regarded as a cavity that confines electron waves along the length axis, with the two ends acting as mirrors to reflect the electron waves back and forth in the longitudinal direction. In this case, the multiploar plasmon modes can be understood as the longitudinal standing waves of electrons. The parameter n denotes the number of nodes within the standing waves along the length direction. However, the scaling law for the Fabry–Pérot cavity, namely, that an integral number of half a wavelength fits into the length of the cavity, is inapplicable to metal nanorods. On the other hand, for these high-aspect-ratio metal nanorods, the conventional quasistatic approximation breaks down due to the retardation effect.[44,45] As a result, the plasmon resonance wavelengths do not show linear dependences on the aspect ratio any more. We therefore endeavored to experimentally determine the relationship between the multipolar plasmon wavelengths and the geometric dimensions of the Ag nanorods. For the purpose of simplicity and conciseness, the Ag nanorods with a fixed diameter

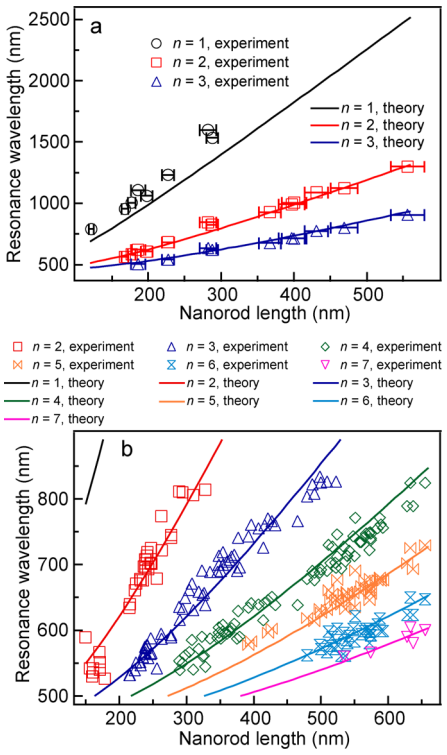

Figure 4. Dependences of the multipolar plasmon wavelengths on the nanorod length. (a) Experimental results measured from the ensemble Ag nanorod samples (symbols) and the empirically predicted values (lines). The error bar width for each experimental point represents one standard deviation of the rod length. (b) Experimental results measured from the individual Ag nanorods deposited on ITO substrates (symbols) and the empirically predicted values (lines). The labeling symbols of the different data sets are provided on the top.

of 38 nm and varying lengths will be considered in the following discussion.

We first examined the relationship at the ensemble level. As shown in Figure 3b, all of the longitudinal plasmon resonance peaks red-shift as the rod length is increased. To get a better view, we further synthesized more than a dozen Ag nanorod samples with their average diameters fixed at 38 nm and lengths varied. The plasmon peak positions were determined from the extinction spectra of the ensemble samples, and plotted as functions of the average rod length in Figure 4a. Each plasmon mode is seen to be variable from the visible to near-infrared region, depending on the mode order and rod length.

The mathematical expression for the dependences of the multipolar plasmon wavelengths on the rod sizes for high-aspect-ratio metal nanostructures has been studied in a few works.[13,14] By combining together electrodynamic simulations and a nanoantenna-standing wave model, an empirical equation has been proposed as follows:[13]

$$\lambda_n = \frac{1}{\beta}\left[\left(\frac{L^2}{n^2\pi^2}\left(A+\frac{B}{D^2}\right)+C\right)\varepsilon_m+\alpha\right]^{1/2} \quad (1)$$

where λ_n is in units of μm and n, L, and D denote the mode order, rod length, and diameter, respectively. ε_m is the dielectric constant of the surrounding medium, which is set to be 1.33[2] for water. $\alpha = 3.7$ and $\beta = 7.25$ μm^{-1} are the material parameters obtained by fitting the real part of the dielectric function of silver according to the Drude–Sommerfeld function of the form $\varepsilon_1 = \alpha - \beta^2\lambda^2$. $A = 2687$ μm^{-2}, $B = 4.4$, and $C = 3.7$ are the fitting coefficients derived from extensive numerical electrodynamic simulations. The multipolar plasmon wavelengths calculated according to eq 1 as functions of the rod length are also plotted in Figure 4a. Our experimental data points, especially those of the higher-order plasmon modes, match well with the predictions based on the empirical equation. The experimental resonance wavelengths of the dipolar plasmon mode ($n = 1$) have the same tendency as the empirical prediction but generally show red shifts of 100–200 nm. This deviation can be ascribed to the difference of the real part of the dielectric function of silver in the near-infrared region (Supporting Information Figure S5) between the experiment data and the Drude–Sommerfeld function used in deriving eq 1. The difference becomes larger with increasing wavelengths. Despite the deviation, eq 1 can still be employed for estimating and predicting the peak positions of the multipolar plasmon modes. A combination of our synthesis method and the empirical equation will enable the production of Ag nanorods with any particular plasmon mode to be at desired wavelengths.

To better understand the dependences of the multipolar plasmon wavelengths on the nanorod length, we measured the dark-field scattering spectra of the individual Ag nanorods deposited on conductive indium tin oxide (ITO)-coated glass slides. Such measurements are also of technological importance, because many applications based on multipolar plasmon resonance are expected to have metal nanostructures supported on substrates. A pattern-matching method was utilized to correlate the scattering spectrum of each Ag nanorod with its SEM image.[46] Figure 5a shows the scattering spectra and SEM images of eight representative Ag nanorods with increasing lengths. For the 161 nm long Ag nanorod, the $n = 1$ peak is located beyond 850 nm and the $n = 2$ peak can be barely seen at 535 nm. For the 225 nm long Ag nanorod, the $n = 2$ peak red-shifts to 671 nm and the $n = 3$ peak shows up at 551 nm. As the rod length is further increased, all multipolar plasmon peaks red-shift and new peaks of higher orders appear. By measuring the geometrical sizes and scattering spectra of more than 100 individual Ag nanorods, the variations of the multipolar plasmon wavelengths as functions of the rod length were obtained (Figure 4b). At the single-particle level, not only the quadrupolar ($n = 2$) and octupolar ($n = 3$) branches but also higher-order ($n = 4, 5, 6, 7$) branches were observed. For even longer Ag nanorods, the higher-order ($n > 7$) peaks

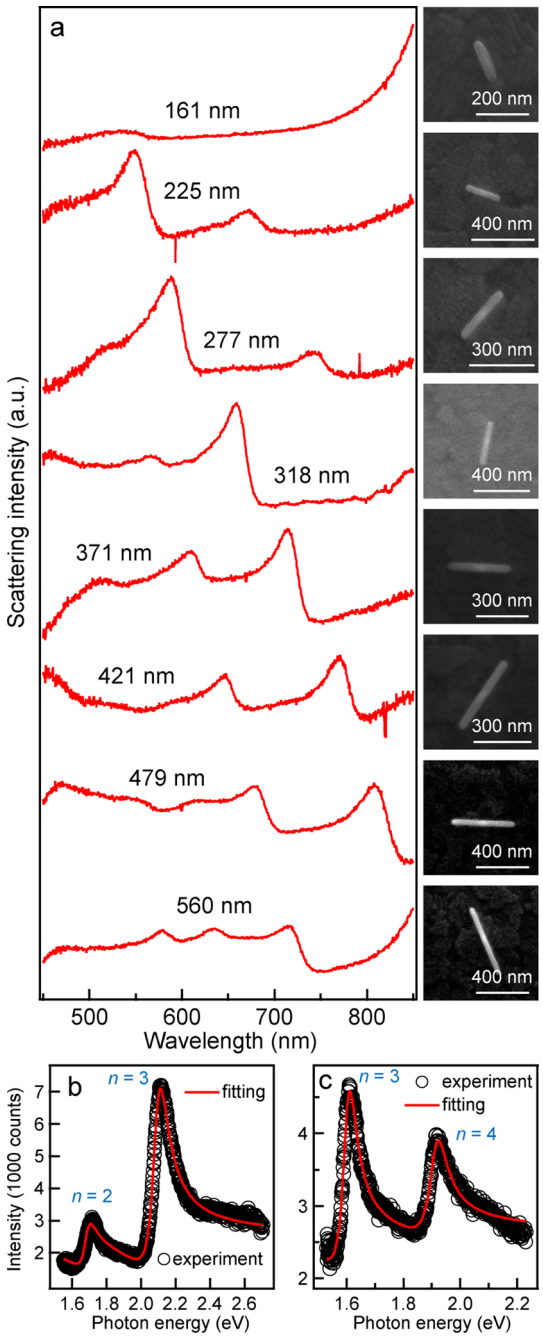

Figure 5. Dark-field scattering spectra of the individual Ag nanorods deposited on ITO substrates. (a) Scattering spectra (left) and the corresponding SEM images (right) of 8 representative Ag nanorods. The scattering spectra were measured with the dark-field objective with a numerical aperture of 0.9. The lengths of the Ag nanorods are provided above the corresponding spectra. (b) Fano-fitting of the experimental scattering spectra of a 262 nm long and a 421 nm long Ag nanorod, respectively. The corresponding coefficients of determination for the fitting are R^2 = 0.99 and 0.97.

were weak and indistinguishable. The Ag nanorods sitting on ITO substrates have a nonuniform surrounding environment, with the top being air and the bottom being ITO. We calculated the multipolar plasmon wavelengths according to eq 1 by setting $\varepsilon_m = 1.32^2 = 1.7424$, which was found to give the best agreement with the experimental data for all multipolar plasmon modes.

We observed that the scattering peaks of higher-order modes are sometimes stronger than those of lower-order modes (Figure 5a). This is different from the case of the ensemble samples. To understand this observation, we measured the single-particle scattering spectra with two dark-field objectives. One has a magnification of 100× and numerical aperture of 0.9, and the other has a magnification of 50× and numerical aperture of 0.5. The incidence light angles relative to the surface normal for the two objectives are 64° and 30°, respectively. As shown in Supporting Information Figure S6, when the objective with the incidence angle of 64° was employed, both odd and even modes were detected. When the objective with the incidence angle of 30° was used, however, only the peaks of the odd modes were clearly observed. In other words, the scattering intensities of the multipolar plasmon modes are angle-dependent, as shown above by the FDTD simulations (Supporting Information Figures S3 and S4).[19] This explains why higher-order modes can be stronger in scattering than lower-order ones. Exploiting such angle-dependent extinction/scattering properties of the Ag nanorods can potentially contribute in the development of devices for light manipulation and fluorescence spectroscopy.[20,21]

Another notable feature of the single-particle scattering spectra is the Fano-like line shape of the higher-order plasmon peaks. A previous study on high-aspect-ratio Au nanorods has shown that the even modes possess a symmetric Lorentzian line shape, while the odd ones display an asymmetric line shape due to the parity-related Fano interference.[7] Another study on low-aspect-ratio Au nanorods shows that the coupling between fat Au nanorods and high-refractive-index substrates also gives rise to Fano interference.[47] In our experiments, all higher-order plasmon peaks were seen to exhibit an asymmetric line shape, with two examples provided in Figure 5b and c, respectively. The measured scattering peaks can be well fitted according to a multipeak Fano function:

$$I_{scat} = A_0 + \sum_i A_i \frac{\left(q_i + \frac{E - E_{res,i}}{\Gamma_i/2}\right)^2}{1 + \left(\frac{E - E_{res,i}}{\Gamma_i/2}\right)^2} (i = 1, 2, \ldots) \quad (2)$$

where A_0 and A_i are fitting coefficients, $E_{res,i}$ and Γ_i are the resonance energy and the line width of the plasmon peak, and q_i is the Fano factor that describes the asymmetry of the plasmon peak. The fitting for the 262 nm long Ag nanorod shown in Figure 5b gives $q_2 = 1.49$, $\Gamma_2 = 83$ meV for the $n = 2$ peak and $q_3 = 2.35$, $\Gamma_3 = 106$ meV for the $n = 3$ peak. For the 421 nm long Ag nanorod shown in Figure 5c, the fitting results are $q_3 = 2.91$, $\Gamma_3 = 58$ meV for the $n = 3$ peak and $q_4 = 2.69$,

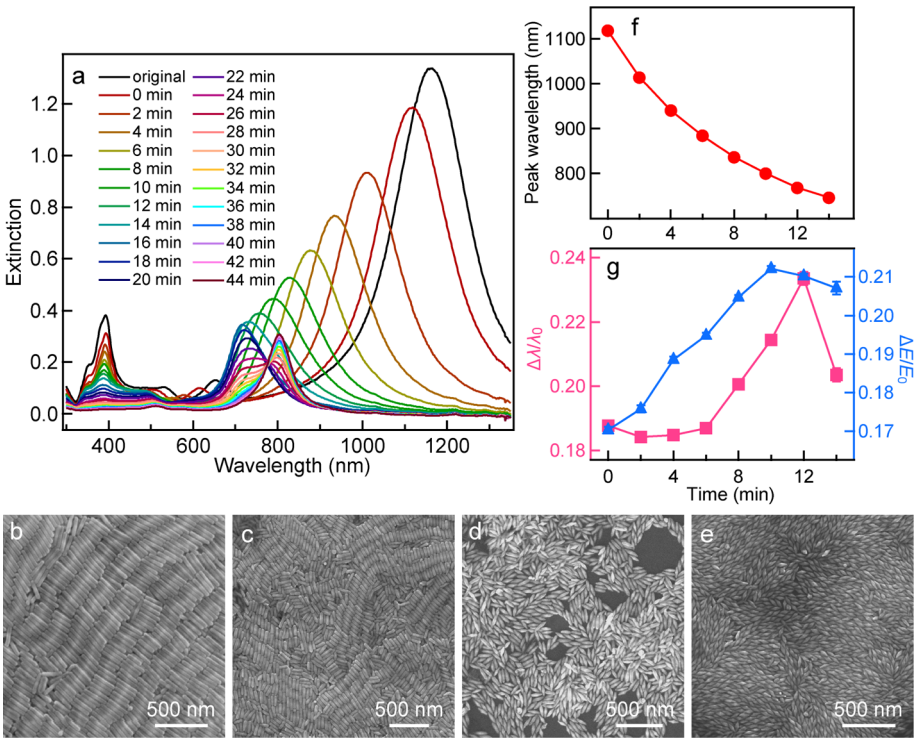

Figure 6. Anisotropic oxidation of the Ag nanorods. (a) Time-dependent extinction spectra of the Ag nanorod solution acquired every 2 min after the addition of the oxidizing agent. (b) SEM image of the starting Ag nanorod sample. (c) SEM image of the sample obtained at the fourth minute. (d) SEM image of the sample obtained at the 22nd minute. (e) SEM image of the sample obtained at the 44th minute. (f) Variation of the wavelength of the $n = 1$ peak during the oxidization process. (g) Variation of the normalized fwhm value in both wavelength and energy of the $n = 1$ peak during the oxidization process. $\Delta\lambda$ and ΔE are the fwhm values in wavelength and energy, respectively, and λ_0 and E_0 are the corresponding peak positions in wavelength and energy.

Γ_4 = 75 meV for the $n = 4$ peak. We found that the asymmetric factor q of the $n = 3$ mode is always larger than those of the other modes. If the high refractive index of the ITO substrate ($n_{ITO} \approx 1.9$) is considered, the asymmetric line shape of the other modes should mainly result from the substrate-induced Fano interference. The more strongly asymmetric line shape of the $n = 3$ mode, however, should arise from a combination of the substrate-induced Fano interference and the parity-related Fano interference. Moreover, the narrow line widths of the higher-order plasmon modes are also noticeable. The line widths obtained from the fitting are close to the full width at half-maximum (fwhm) values determined manually from the scattering peaks. The fwhm values of the longitudinal dipolar plasmon mode supported by single Ag nanorods are typically 150−250 meV within the same spectral region.[48] The reduced line widths of the multipolar plasmon modes are due to their smaller radiative decay.[6] The Fano shape and narrower line widths of the multipolar plasmon modes are attractive for developing highly sensitive detection devices as well as for exploring Fano resonance-based optical applications.

Anisotropic Oxidation. The plasmon wavelength of the Ag nanorod sample can be synthetically tailored not only in the Ag overgrowth process but also after growth. We further demonstrated the fine-tuning of the plasmon wavelength of the Ag nanorod sample by anisotropic mild oxidation at room temperature. This facile approach, which is applicable for the adjustment of the dipolar as well as multipolar plasmon wavelengths, offers more convenience and controllability for practical applications.

The starting Ag nanorod sample for anisotropic oxidation was prepared following the procedure described above. The average length and diameter are 203 ± 12 nm and 38 ± 1 nm, respectively. For oxidation, the Ag nanorod solution was mixed with small amounts of $NH_3 \cdot H_2O$ and H_2O_2 in the presence of CTAB. H_2O_2 functioned as the oxidizing agent. $NH_3 \cdot H_2O$ was used to increase the solubility of Ag^+ ions through the formation of $[Ag(NH_3)_2]^+$ complex ions, therefore facilitating the oxidation reaction process. The oxidation process was monitored in real time by acquiring the extinction spectra of the Ag nanorod solution every 2 min after the oxidizing agent was added, as shown in Figure 6a. The starting Ag nanorod sample (Figure 6b) exhibits the $n = 1$ peak at 1163 nm, $n = 2$ peak at 654 nm, $n = 3$ peak at 530 nm, and transverse plasmon peak at 390 nm. In the beginning, all of the longitudinal plasmon peaks ($n = 1, 2, 3$) blueshift and decrease in intensity, while the transverse plasmon peak stays at 390 nm and decreases gradually in intensity. The spectral evolution suggests that the Ag

nanorods are shortened but maintain a constant diameter. The size variation is confirmed by the size measurements performed on an oxidized sample (Figure 6c) taken out of the reaction solution at the fourth minute. The resultant average length and diameter are 134 ± 13 nm and 38 ± 1 nm, respectively. Upon further oxidation, the $n = 1$ peak stops at 717 nm without further blue-shifting and begins to red-shift instead, displaying an asymmetric line shape. Meanwhile, the transverse plasmon peak at 390 nm vanishes gradually. Figure 6d and Supporting Information Figure S7 show the SEM and TEM images of the sample at this stage. It is an intermediate stage during the transition from Ag nanorods to Au NBPs. Subsequently, a shoulder around 800 nm, arising from the bare Au NBPs, appears and becomes dominant finally. Figure 6e shows the SEM image of the end product, the bare Au NBPs, from the oxidation process.

The wavelengths of the $n = 1$ peak were extracted from the time-dependent extinction spectra and plotted as a function of time in Figure 6f. It shows clearly the gradual blue shift in the early stage of the oxidation process. Figure 6g shows the evolution of the fwhm values in both wavelength and energy. The fwhm values were obtained by fitting the $n = 1$ peak with the Lorentzian function. They have been normalized against the peak wavelengths or energies to remove the intrinsic changes caused by the peak shifts in energy.[49] During the first 12 min, the normalized fwhm values were seen to increase gradually, suggesting an increase in the standard deviation of the average length with oxidation. After 12 min, the normalized fwhm value begins to decrease. At this stage, the Ag shell outside the Au NBP becomes very thin. The nanostructures start to lose the well-defined rod shape. As a result, the effect of the Au NBP on the plasmon resonance modes shows up gradually and complicates the variation trend of the fwhm value. This is why the peak wavelengths in Figure 6f and the fwhm values in Figure 6g are plotted only within a time period of 14 min. We are currently studying the plasmonic evolution behaviors when only a small amount of silver is overgrown on Au NBPs. The results will be reported soon in a separate study.

To the best of our knowledge, our study is the first in realizing anisotropic oxidation of Ag nanorods for adjusting the rod length and therefore the wavelengths of the different plasmon modes. There are mainly two reasons for the anisotropic oxidation of the Ag nanorods at their ends. First, the smaller packing density of the CTAB molecules at the two ends of the nanorods relative to that at the side allows for the preferential oxidization at the ends.[39] Second, the Ag nanorods are enclosed by {100} facets at the side.[33,36,37] The side {100} facets can be greatly stabilized in the presence of halide ions.[38] On the other hand, for the example presented in Figure 6, a relatively short Ag nanorod sample was chosen, and an excess amount of the oxidizing agent was added in order to provide a clear overview of the entire oxidation process in a relatively short period of time. Our method is applicable for longer Ag nanorods as well. In addition, the reaction rate is actually controllable by varying the amount of the oxidizing agent, the reaction temperature, and surfactant concentration.[39] As a result, fine adjustment of the rod length and, therefore, the peak positions of any particular longitudinal plasmon mode, can be achieved by slowing down the reaction rate.

Hollow AuAg Nanostructures and Ag Nanowires. We finally demonstrated two types of metal nanostructures that are highly related to the Ag nanorods. One is hollow AuAg nanostructures, and the other is Ag nanowires. The successful production of these two types of metal nanostructures is a further proof of the versatility of our Au NBP-directed growth method.

Hollow AuAg nanostructures have been examined as an attractive agent for photothermal therapy, drug delivery, and optical imaging. A variety of hollow metal nanostructures have been synthesized through galvanic replacement reaction.[50] Similarly, in our study, we prepared elongated hollow AuAg nanostructures by adding $HAuCl_4$ solution (0.5 mM) dropwise into the Ag nanorod solution at room temperature. Since the reduction of one Au(III) ion requires the oxidation of three Ag atoms, the Ag nanorods become hollow gradually. Supporting Information Figure S8 shows the extinction spectra and SEM and TEM images of the hollow nanostructure samples produced by adding different amounts of $HAuCl_4$ relative to the Ag nanorod amount. The amount of $HAuCl_4$ was found to be crucial for producing the hollow nanostructures. A small amount of $HAuCl_4$ leads to incomplete reaction (Supporting Information Figure S8b and c). On the contrary, if an excess amount of $HAuCl_4$ is supplied, the shell tends to fragment into small pieces (Supporting Information Figure S8f and g). In our experiments, the hollow nanostructures could be produced when the molar ratio of $HAuCl_4$ and Ag in the reaction solution was estimated to be 1:3 to 1:5 by inductively coupled plasma atomic emission spectrometry (ICP-AES) measurements. The Au-to-Ag atomic ratios of the as-prepared hollow nanostructures were measured to be around 60:40 by energy-dispersive X-ray (EDX) analysis on the SEM system, indicating that the Ag segment was not completely replaced by gold. In other words, the shell of the hollow nanostructure could be AuAg alloy.[50] The uniform Ag nanorods with controllable sizes allow for the synthesis of size-tunable hollow AuAg nanostructures. Figure 7a–f show three examples of such hollow nanostructures that were made from the Ag nanorod samples shown in Figure 2a–c. The produced hollow nanostructures, with each consisting of a hollow nanotube and a single Au NBP at the

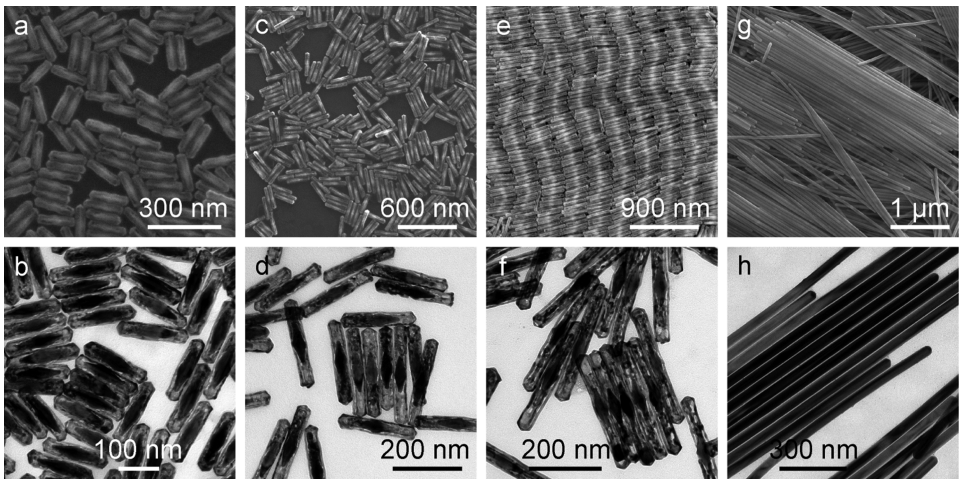

Figure 7. Hollow AuAg nanostructures and Ag nanowires. In the top and bottom rows are the SEM and TEM images, respectively. (a−f) Three AuAg nanostructure samples prepared respectively from the three Ag nanorod samples shown in Figure 2a−c. The average lengths and diameters of the three hollow nanostructure samples are 172 ± 9 nm/41 ± 2 nm, 250 ± 18 nm/42 ± 2 nm, and 337 ± 23 nm/42 ± 2 nm, respectively. The molar ratios between $HAuCl_4$ and Ag in the galvanic replacement reaction solutions were estimated to be 1:3, 1:4, and 1:5, respectively. (g, h) Ag nanowires grown with the 900 nm NBPs as the cores. The average diameter is 46 ± 2 nm.

center, maintain the rod shape but have slightly enlarged dimensions. Their extinction spectra (Supporting Information Figure S9a) show that the longitudinal plasmon peak red-shifts as the particle length is increased.

Ag nanowires have recently attracted much attention because of their ability to support propagating surface plasmon resonance[51] as well as their fabrication into transparent conductive electrodes.[52,53] In our experiment, Ag nanowires can be easily prepared by repeating the Ag overgrowth process several times. Similar to the Ag nanorods, the diameters of the Ag nanowires can be roughly controlled by choosing Au NBPs with different sizes. Additional Ag atoms are deposited onto the Ag nanorods along the longitudinal direction without affecting the diameters. As an example, we synthesized a nanowire sample with an average length of ~4 μm (Figure 7g) by repeating the Ag overgrowth process three times. As shown in Figure 7h, the Ag nanowires are highly uniform in diameter. The extinction spectrum (Supporting Information Figure S9b) shows only the sharp transverse plasmon peak and the shoulder due to the plasmon resonance of bulk silver, suggesting the high purity of the nanowire product. We have no doubt that even longer Ag nanowires can be prepared with our approach by increasing the number of overgrowth cycles. Compared with other methods,[41,42,53] our method shows flexibility and advantage in control of the diameters and lengths of Ag nanowires.

CONCLUSIONS

In summary, we have successfully demonstrated a facile approach to the preparation of high-aspect-ratio Ag nanorods on the basis of Au NBP-directed Ag overgrowth. We have synthesized Ag nanorods with diameters ranging from ~20 to ~50 nm and lengths ranging from ~150 to ~550 nm. The aspect ratios of these Ag nanorods are varied over a wide range from ~3 to ~30. The FDTD simulations indicate that the effect of the Au NBP core on the plasmon properties of the Ag nanorod is negligible, so that the Au NBP-directed Ag nanorods can be regarded as pure Ag nanorods plasmonically. The high aspect ratios, high purity, and high dimensional uniformity of the Ag nanorods allow for the observation of well-separated multipolar plasmon modes in the colloidal suspensions. The length-dependent multipolar plasmon wavelengths have been studied experimentally at both the ensemble and single-particle levels. The results are in good agreement with the predictions based on the reported empirical equation. We have further demonstrated anisotropic oxidation of the Ag nanorods and the transformation of the Ag nanorods into hollow AuAg nanostructures and long Ag nanowires. The anisotropic oxidation offers an alternative means for finely tuning the wavelength of the desired longitudinal plasmon mode. We expect our Ag nanorods with well-controlled multipolar plasmon modes to function as an attractive and powerful building unit in designing multipolar plasmon-based devices and metamaterials.

METHODS

Chemicals. Gold chloride trihydrate ($HAuCl_4 \cdot 3H_2O$, 99%), sodium borohydride ($NaBH_4$, 98%), trisodium citrate (99%), ascorbic acid (99%), and silver nitrate ($AgNO_3$, 99%) were purchased from Sigma-Aldrich. CTAB (98%) was obtained from Alfa Aesar. CTAC (97%) and H_2O_2 solution (30 wt %) were purchased from Aladdin

Chemical. $NH_3 \cdot H_2O$ solution (25 wt %) and HCl solution (5 M) were ordered from E. Merck and Scharlab, respectively. Deionized water with a resistivity of 18.2 MΩ cm obtained from a Direct-Q 5 UV water purification system was used in all experiments.

Preparation of the Au NBPs. The Au NBP samples were prepared using the seed-mediated growth method, as described in previous works.[33,34] Briefly, a freshly prepared, ice-cold $NaBH_4$ solution (0.01 M, 0.15 mL) was mixed with an aqueous solution composed of $HAuCl_4$ (0.01 M, 0.125 mL), trisodium citrate (0.01 M, 0.25 mL), and water (9.625 mL) under vigorous stirring. The resultant seed solution was kept at room temperature for 2 h. The as-prepared seed solution (0.1−2 mL) was injected into a growth solution that was made of CTAB solution (0.1 M, 40 mL), $HAuCl_4$ (0.01 M, 2 mL), $AgNO_3$ (0.01 M, 0.4 mL), HCl (1 M, 0.8 mL), and ascorbic acid (0.1 M, 0.32 mL) in advance, followed by gentle inversion mixing for 10 s. The reaction solution was left undisturbed overnight at room temperature. The highly pure Au NBP samples were obtained by using a depletion-induced separation method, as reported in our recent study.[35] The product was dispersed in a CTAB solution (10 mM) for further use. For the 650, 800, and 900 nm NBP samples used in our experiments, the extinction values per 0.5 cm at the longitudinal plasmon peaks were 0.8, 1.7, and 2.0, respectively. The corresponding particle concentrations of the three Au NBP samples were estimated to be 1.8×10^{11}, 4.1×10^{10}, and 2.7×10^{10} particles mL^{-1}, respectively. The estimation was based on the simulated extinction cross-section of a single Au NBP and the extinction value of the Au NBP solution.

Gold NBP-Directed Growth of Silver Nanorods and Silver Nanowires. The Au NBP solution (10 mL) was centrifuged at 5000−9000 rpm for 15 min. The precipitate was redispersed in CTAC (0.08 M, 30 mL), followed by subsequent addition and mixing of $AgNO_3$ (0.01 M) and ascorbic acid (0.1 M). For the three Ag nanorod samples shown in Figure 1e−g, the volumes of the $AgNO_3$ solution were 2, 4, and 5 mL, respectively. For the five Ag nanorod samples shown in Figure 2, the volumes of the $AgNO_3$ solution were 0.8, 2, 4, 8, and 12 mL, respectively. The volume of the ascorbic acid solution was half of the $AgNO_3$ solution for each overgrowth. The mixture solution was placed in an air-bath shaker (60 °C, 120 rpm) and kept for 4.5 h, during which silver was overgrown on Au NBPs to form Ag nanorods. The resultant samples were centrifuged at 3000−5000 rpm for 15 min. The precipitates were redispersed in water (30 mL) for further use. For preparing Ag nanowires with lengths above 1 μm, the overgrowth process was repeated several times. The volume of the $AgNO_3$ solution was 8 mL in each overgrowth cycle for the Ag nanowire sample shown in Figure 7g.

Anisotropic Oxidation. The as-prepared Ag nanorod sample (2 mL) was mixed with water (1 mL) and CTAB (0.1 M, 0.6 mL). After $NH_3 \cdot H_2O$ (25 wt %, 0.2 mL) and H_2O_2 (6 wt %, 5 μL) were added at room temperature, the solution mixture was shaken and placed into the chamber of a spectrophotometer for real-time measurements of the extinction spectra. To obtain the samples at the intermediate oxidation stages, a portion (1 mL) of the reaction solution was taken out and rapidly subjected to centrifugation to stop the oxidation.

Preparation of the Hollow AuAg Nanostructures. The hollow AuAg nanostructures were prepared through a galvanic replacement reaction between the Au NBP-directed Ag nanorods and $HAuCl_4$ in aqueous solutions at room temperature. Briefly, a mixture of the as-prepared Ag nanorod solution (2 mL) and CTAB (0.1 M, 0.2 mL) was kept under vigorous stirring. Different volumes of $HAuCl_4$ (0.5 mM) were then added dropwise. For the three samples shown in Figure 7, the volumes of the $HAuCl_4$ solution were 178, 340, and 550 μL, respectively. After 1 h, the reaction was stopped by centrifugation at 3000−5000 rpm for 7 min. The hollow nanostructures were washed by water twice to remove AgBr and excess Au-based ions.

Instrumentation. Extinction spectra were recorded on a Hitachi U-3501 ultraviolet/visible/near-infrared spectrophotometer with standard 0.5 cm cuvettes. SEM imaging was performed on an FEI Quanta 400 FEG microscope operated at 20 kV. TEM imaging was carried out on an FEI Tecnai Spirit 12 microscope operated at 120 kV. Elemental mapping was carried out on an FEI Tecnai F20 microscope equipped with an Oxford EDX analysis system. ICP-AES measurements were performed on a PerkinElmer Optima 4300DV system. Single-particle dark-field scattering spectra were recorded on an upright optical microscope (Olympus, BX60) that was integrated with a quartz−tungsten−halogen lamp (100 W), a monochromator (Acton, SpectraPro 2360i), and a charge-coupled device camera (Princeton Instruments, Pixis 400). During the measurements, the camera was thermoelectrically cooled to −70 °C. Two dark-field objectives (100×, numerical aperture 0.9; 50×, numerical aperture 0.5) were employed for both exciting the individual nanorods with the white light and collecting the scattered light. The scattering spectrum from an individual nanorod was corrected by first subtracting the background spectrum taken from the adjacent region without any nanoparticles and then dividing it with a precalibrated response curve of the entire optical system. The exposure time was set at 60 s.

FDTD Simulations. The simulations were performed using FDTD Solutions 8.7 developed by Lumerical Solutions. In the simulations, an electromagnetic plane wave in the wavelength range from 300 to 1800 nm was launched into a box containing a target Ag nanorod. A mesh size of 1 nm was employed in calculating the extinction spectra of the Ag nanorods, and 0.5 nm was employed in calculating the charge distribution contours. The refractive index of the surrounding medium was set to 1.33, which is the refractive index of water. The dielectric function of gold was obtained by fitting the measured data of Johnson and Christy, and that of silver was fitted from Palik's data. Each Ag nanorod was modeled as a cylinder with two hemispherical ends. The Au NBP core was modeled as two base-connected circular cones with the tips spherically truncated at a radius of 5 nm. The geometrical parameters were set to be as close as possible to the average sizes measured from the TEM images. Since the even-parity plasmon modes can be excited only by excitation light that is nonperpendicular to the rod length axis, different excitation directions and polarizations were considered by setting the excitation light wavevector at varying angles relative to the rod length axis and setting the excitation polarization to be either within (p-polarized) or perpendicular (s-polarized) to the plane that is determined by the rod length axis and the excitation light direction. The final simulated extinction spectrum C_{ext} was then obtained by averaging according to

$$C_{ext} = \left\langle \frac{1}{2} [C^{p}_{ext}(\theta) + C^{s}_{ext}(\theta)] \right\rangle_{\theta, \phi} \quad (3)$$

The averaging in eq 3 was based on a spherical coordinate system. In the coordinate system, θ, the polar angle, representing the angle between the excitation wavevector and the direction normal to the rod length axis, was set as 0°, 15°, 30°, 45°, 60°, 75°, and 90°. φ was the azimuthal angle, which was introduced solely for proper averaging based on the integration on a spherical surface.

Conflict of Interest: The authors declare no competing financial interest.

Acknowledgment. This work was supported by Hong Kong RGC Theme-based Research Scheme (ref. no. T23-407-13N).

Supporting Information Available: SEM images of the Au NBP samples; HAADF-STEM image and elemental mapping images of the Ag nanorods; additional FDTD simulation details; angle-dependent dark-field scattering spectra; TEM image of the sample obtained at an intermediate stage during anisotropic oxidation; TEM images of the hollow AuAg nanostructures; extinction spectra of the hollow AuAg nanostructures and the Ag nanowires. The Supporting Information is available free of charge on the ACS Publications website at DOI: 10.1021/acsnano.5b02622.

REFERENCES AND NOTES

1. Giannini, V.; Fernández-Domínguez, A. I.; Heck, S. C.; Maier, S. A. Plasmonic Nanoantennas: Fundamentals and Their Use in Controlling the Radiative Properties of Nanoemitters. *Chem. Rev.* **2011**, *111*, 3888–3912.

2. Mayer, K. M.; Hafner, J. H. Localized Surface Plasmon Resonance Sensors. *Chem. Rev.* **2011**, *111*, 3828–3857.
3. Jiang, R. B.; Li, B. X.; Fang, C. H.; Wang, J. F. Metal/Semiconductor Hybrid Nanostructures for Plasmon-Enhanced Applications. *Adv. Mater.* **2014**, *26*, 5274–5309.
4. Lal, S.; Grady, N. K.; Kundu, J.; Levin, C. S.; Lassiter, J. B.; Halas, N. J. Tailoring Plasmonic Substrates for Surface Enhanced Spectroscopies. *Chem. Soc. Rev.* **2008**, *37*, 898–911.
5. Taminiau, T. H.; Stefani, F. D.; van Hulst, N. F. Optical Nanorod Antennas Modeled as Cavities for Dipolar Emitters: Evolution of Sub- and Super-Radiant Modes. *Nano Lett.* **2011**, *11*, 1020–1024.
6. Zhang, S. P.; Chen, L.; Huang, Y. Z.; Xu, H. X. Reduced Linewidth Multipolar Plasmon Resonances in Metal Nanorods and Related Applications. *Nanoscale* **2013**, *5*, 6985–6991.
7. Verellen, N.; López-Tejeira, F.; Paniagua-Domínguez, R.; Vercruysse, D.; Denkova, D.; Lagae, L.; Van Dorpe, P.; Moshchalkov, V. V.; Sánchez-Gil, J. A. Mode Parity-Controlled Fano- and Lorentz-like Line Shapes Arising in Plasmonic Nanorods. *Nano Lett.* **2014**, *14*, 2322–2329.
8. Martin, J.; Kociak, M.; Mahfoud, Z.; Proust, J.; Gérard, D.; Plain, J. High-Resolution Imaging and Spectroscopy of Multipolar Plasmonic Resonances in Aluminum Nanoantennas. *Nano Lett.* **2014**, *14*, 5517–5523.
9. Nicoletti, O.; Wubs, M.; Mortensen, N. A.; Sigle, W.; van Aken, P. A.; Midgley, P. A. Surface Plasmon Modes of a Single Silver Nanorod: An Electron Energy Loss Study. *Opt. Express* **2011**, *19*, 15371–15379.
10. Guiton, B. S.; Iberi, V.; Li, S. Z.; Leonard, D. N.; Parish, C. M.; Kotula, P. G.; Varela, M.; Schatz, G. C.; Pennycook, S. J.; Camden, J. P. Correlated Optical Measurements and Plasmon Mapping of Silver Nanorods. *Nano Lett.* **2011**, *11*, 3482–3488.
11. Douillard, L.; Charra, F.; Korczak, Z.; Bachelot, R.; Kostcheev, S.; Lerondel, G.; Adam, P.-M.; Royer, P. Short Range Plasmon Resonators Probed by Photoemission Electron Microscopy. *Nano Lett.* **2008**, *8*, 935–940.
12. Dorfmüller, J.; Vogelgesang, R.; Weitz, R. T.; Rockstuhl, C.; Etrich, C.; Pertsch, T.; Lederer, F.; Kern, K. Fabry-Pérot Resonances in One-Dimensional Plasmonic Nanostructures. *Nano Lett.* **2009**, *9*, 2372–2377.
13. Encina, E. R.; Coronado, E. A. Resonance Conditions for Multipole Plasmon Excitations in Noble Metal Nanorods. *J. Phys. Chem. C* **2007**, *111*, 16796–16801.
14. Khlebtsov, B. N.; Khlebtsov, N. G. Multipole Plasmons in Metal Nanorods: Scaling Properties and Dependence on Particle Size, Shape, Orientation, and Dielectric Environment. *J. Phys. Chem. C* **2007**, *111*, 11516–11527.
15. López-Tejeira, F.; Paniagua-Domínguez, R.; Sánchez-Gil, J. A. High-Performance Nanosensors Based on Plasmonic Fano-like Interference: Probing Refractive Index with Individual Nanorice and Nanobelts. *ACS Nano* **2012**, *6*, 8989–8996.
16. Paul, A.; Solis, D., Jr.; Bao, K.; Chang, W.-S.; Nauert, S.; Vidgerman, L.; Zubarev, E. R.; Nordlander, P.; Link, S. Identification of Higher Order Long-Propagation-Length Surface Plasmon Polariton Modes in Chemically Prepared Gold Nanowires. *ACS Nano* **2012**, *6*, 8105–8113.
17. López-Tejeira, F.; Paniagua-Domínguez, R.; Rodríguez-Oliveros, R.; Sánchez-Gil, J. A. Fano-Like Interference of Plasmon Resonances at a Single Rod-Shaped Nanoantenna. *New J. Phys.* **2012**, *14*, 023035.
18. Collins, S. M.; Nicoletti, O.; Rossouw, D.; Ostasevicius, T.; Midgley, P. A. Excitation Dependent Fano-Like Interference Effects in Plasmonic Silver Nanorods. *Phys. Rev. B: Condens. Matter Mater. Phys.* **2014**, *90*, 155419.
19. Encina, E. R.; Coronado, E. A. Plasmonic Nanoantennas: Angular Scattering Properties of Multipole Resonances in Noble Metal Nanorods. *J. Phys. Chem. C* **2008**, *112*, 9586–9594.
20. Giannini, V.; Vecchi, G.; Rivas, J. G. Lighting Up Multipolar Surface Plasmon Polaritons by Collective Resonances in Arrays of Nanoantennas. *Phys. Rev. Lett.* **2010**, *105*, 266801.
21. Curto, A. G.; Taminiau, T. H.; Volpe, G.; Kreuzer, M. P.; Quidant, R.; van Hulst, N. F. Multipolar Radiation of Quantum Emitters with Nanowire Optical Antennas. *Nat. Commun.* **2013**, *4*, 1750.
22. Day, J. K.; Large, N.; Nordlander, P.; Halas, N. J. Standing Wave Plasmon Modes Interact in an Antenna-Coupled Nanowire. *Nano Lett.* **2015**, *15*, 1324–1330.
23. Schider, G.; Krenn, J. R.; Hohenau, A.; Ditlbacher, H.; Leitner, A.; Aussenegg, F. R.; Schaich, W. L.; Puscasu, I.; Monacelli, B.; Boreman, G. Plasmon Dispersion Relation of Au and Ag Nanowires. *Phys. Rev. B: Condens. Matter Mater. Phys.* **2003**, *68*, 155427.
24. Laurent, G.; Félidj, N.; Aubard, J.; Lévi, G.; Krenn, J. R.; Hohenau, A.; Schider, G.; Leitner, A.; Aussenegg, F. R. Evidence of Multipolar Excitations in Surface Enhanced Raman Scattering. *Phys. Rev. B: Condens. Matter Mater. Phys.* **2005**, *71*, 045430.
25. Wei, H.; Reyes-Coronado, A.; Nordlander, P.; Aizpurua, J.; Xu, H. X. Multipolar Plasmon Resonances in Individual Ag Nanorice. *ACS Nano* **2010**, *4*, 2649–2654.
26. Imura, K.; Nagahara, T.; Okamoto, H. Near-Field Optical Imaging of Plasmon Modes in Gold Nanorods. *J. Chem. Phys.* **2005**, *122*, 154701.
27. Huang, H. J.; Yu, C. P.; Chang, H. C.; Chiu, K. P.; Chen, H. M.; Liu, R. S.; Tsai, D. P. Plasmonic Optical Properties of a Single Gold Nano-rod. *Opt. Express* **2007**, *15*, 7132–7139.
28. Payne, E. K.; Shuford, K. L.; Park, S.; Schatz, G. C.; Mirkin, C. A. Multipole Plasmon Resonances in Gold Nanorods. *J. Phys. Chem. B* **2006**, *110*, 2150–2154.
29. Khanal, B. P.; Zubarev, E. R. Purification of High Aspect Ratio Gold Nanorods: Complete Removal of Platelets. *J. Am. Chem. Soc.* **2008**, *130*, 12634–12635.
30. Liang, H. Y.; Yang, H. X.; Wang, W. Z.; Li, J. Q.; Xu, H. X. High-Yield Uniform Synthesis and Microstructure-Determination of Rice-Shaped Silver Nanocrystals. *J. Am. Chem. Soc.* **2009**, *131*, 6068–6069.
31. Pietrobon, B.; McEachran, M.; Kitaev, V. Synthesis of Size-Controlled Faceted Pentagonal Silver Nanorods with Tunable Plasmonic Properties and Self-Assembly of These Nanorods. *ACS Nano* **2009**, *3*, 21–26.
32. Zhang, J.; Langille, M. R.; Mirkin, C. A. Synthesis of Silver Nanorods by Low Energy Excitation of Spherical Plasmonic Seeds. *Nano Lett.* **2011**, *11*, 2495–2498.
33. Liu, M. Z.; Guyot-Sionnest, P. Mechanism of Silver(I)-Assisted Growth of Gold Nanorods and Bipyramids. *J. Phys. Chem. B* **2005**, *109*, 22192–22200.
34. Kou, X. S.; Ni, W. H.; Tsung, C.-K.; Chan, K.; Lin, H.-Q.; Stucky, G. D.; Wang, J. F. Growth of Gold Bipyramids with Improved Yield and Their Curvature-Directed Oxidation. *Small* **2007**, *3*, 2103–2113.
35. Li, Q.; Zhuo, X. L.; Li, S.; Ruan, Q. F.; Xu, Q.-H.; Wang, J. F. Production of Monodisperse Gold Nanobipyramids with Number Percentages Approaching 100% and Evaluation of Their Plasmonic Properties. *Adv. Opt. Mater.* **2015**, *3*, 801.
36. Li, Q.; Jiang, R. B.; Ming, T.; Fang, C. H.; Wang, J. F. Crystalline Structure-Dependent Growth of Bimetallic Nanostructures. *Nanoscale* **2012**, *4*, 7070–7077.
37. Sun, Y. G.; Mayers, B.; Herricks, T.; Xia, Y. N. Polyol Synthesis of Uniform Silver Nanowires: A Plausible Growth Mechanism and the Supporting Evidence. *Nano Lett.* **2003**, *3*, 955–960.
38. Gómez-Graña, S.; Goris, B.; Altantzis, T.; Fernández-López, C.; Carbó-Argibay, E.; Guerrero-Martínez, A.; Almora-Barrios, N.; López, N.; Pastonriza-Santos, I.; Pérez-Juste, J.; et al. Au@Ag Nanoparticles: Halides Stabilize {100} Facets. *J. Phys. Chem. Lett.* **2013**, *4*, 2209–2216.
39. Tsung, C.-K.; Kou, X. S.; Shi, Q. H.; Zhang, J. P.; Yeung, M. H.; Wang, J. F.; Stucky, G. D. Selective Shortening of Single-Crystalline Gold Nanorods by Mild Oxidation. *J. Am. Chem. Soc.* **2006**, *128*, 5352–5353.
40. Park, K.; Koerner, H.; Vaia, R. A. Depletion-Induced Shape and Size Selection of Gold Nanoparticles. *Nano Lett.* **2010**, *10*, 1433–1439.

41. Sun, Y. G.; Xia, Y. N. Large-Scale Synthesis of Uniform Silver Nanowires through a Soft, Self-Seeding, Polyol Process. *Adv. Mater.* **2002**, *14*, 833–837.
42. Sun, Y. G.; Yin, Y. D.; Mayers, B. T.; Herricks, T.; Xia, Y. N. Uniform Silver Nanowires Synthesis by Reducing $AgNO_3$ with Ethylene Glycol in the Presence of Seeds and Poly-(Vinyl Pyrrolidone). *Chem. Mater.* **2002**, *14*, 4736–4745.
43. Jiang, R. B.; Chen, H. J.; Shao, L.; Li, Q.; Wang, J. F. Unraveling the Evolution and Nature of the Plasmons in (Au Core)−(Ag Shell) Nanorods. *Adv. Mater.* **2012**, *24*, OP200–OP207.
44. Bryant, G. W.; García de Abajo, F. J.; Aizpurua, J. Mapping the Plasmon Resonances of Metallic Nanoantennas. *Nano Lett.* **2008**, *8*, 631–636.
45. Slaughter, L. S.; Chang, W.-S.; Swanglap, P.; Tcherniak, A.; Khanal, B. P.; Zubarev, E. R.; Link, S. Single-Particle Spectroscopy of Gold Nanorods beyond the Quasi-Static Limit: Varying the Width at Constant Aspect Ratio. *J. Phys. Chem. C* **2010**, *114*, 4934–4938.
46. Chen, H. J.; Sun, Z. H.; Ni, W. H.; Woo, K. C.; Lin, H.-Q.; Sun, L. D.; Yan, C. H.; Wang, J. F. Plasmon Coupling in Clusters Composed of Two-Dimensionally Ordered Gold Nanocubes. *Small* **2009**, *5*, 2111–2119.
47. Chen, H. J.; Shao, L.; Ming, T.; Woo, K. C.; Man, Y. C.; Wang, J. F.; Lin, H.-Q. Observation of the Fano Resonance in Gold Nanorods Supported on High-Dielectric-Constant Substrates. *ACS Nano* **2011**, *5*, 6754–6763.
48. Jakab, A.; Rosman, C.; Khalavka, Y.; Becker, J.; Trügler, A.; Hohenester, U.; Sönnichsen, C. Highly Sensitive Plasmonic Silver Nanorods. *ACS Nano* **2011**, *5*, 6880–6885.
49. Sönnichsen, C.; Franzl, T.; Wilk, T.; von Plessen, G.; Feldmann, J.; Wilson, O.; Mulvaney, P. Drastic Reduction of Plasmon Damping in Gold Nanorods. *Phys. Rev. Lett.* **2002**, *88*, 077402.
50. Xia, X. H.; Wang, Y.; Ruditskiy, A.; Xia, Y. N. 25th Anniversary Article: Galvanic Replacement: A Simple and Versatile Route to Hollow Nanostructures with Tunable and Well-Controlled Properties. *Adv. Mater.* **2013**, *25*, 6313–6333.
51. Xiong, X.; Zou, C.-L.; Ren, X.-F.; Liu, A.-P.; Ye, Y.-X.; Sun, F.-W.; Guo, G.-C. Silver Nanowires for Photonics Applications. *Laser Photonics Rev.* **2013**, *7*, 901–919.
52. De, S.; Higgins, T. M.; Lyons, P. E.; Doherty, E. M.; Nirmalraj, P. N.; Blau, W. J.; Boland, J. J.; Coleman, J. N. Silver Nanowire Networks as Flexible, Transparent, Conducting Films: Extremely High DC to Optical Conductivity Ratios. *ACS Nano* **2009**, *3*, 1767–1774.
53. Hu, L. B.; Kim, H. S.; Lee, J.-Y.; Peumans, P.; Cui, Y. Scalable Coating and Properties of Transparent, Flexible, Silver Nanowire Electrodes. *ACS Nano* **2010**, *4*, 2955–2963.